Metals **2015**, *5*, 1971-1983; doi:10.3390/met5041971

OPEN ACCESS

metals

ISSN 2075-4701

www.mdpi.com/journal/metals/

Article

Investigation of the Undercoolability of Ni-Based Alloys Using High Temperature Thermal Analysis

Samuel Bogner *, Elvira Ivanova, Marcel Müller, Fu Wang, Dexin Ma and Andreas Bührig-Polaczek

Foundry-Institute, Rheinisch-Westfälische Technische Hochschule (RWTH) Aachen University, Intzestraße 5, 52072 Aachen, Germany; E-Mails: e.ivanova@gi.rwth-aachen.de (E.I.); marcel.mueller2@rwth-aachen.de (M.M.); f.wang@gi.rwth-aachen.de (F.W.); d.ma@gi.rwth-aachen.de (D.M.); sekretariat@gi.rwth-aachen.de (A.B.-P.)

***** Author to whom correspondence should be addressed; E-Mail: s.bogner@gi.rwth-aachen.de; Tel.: +49-241-80-97144; Fax: +49-241-80-38578.

Academic Editor: Johan Moverare

Received: 21 August 2015 / Accepted: 20 October 2015 / Published: 26 October 2015

Abstract: During the single crystal (SX) solidification of turbine blades, grain defects can form in the platform regions which have abruptly varying cross-sections. A high undercoolability of a Ni-based alloy prevents the growth of stray grains in the thermally undercooled platform area. To evaluate the undercoolability of different Ni-based alloys, temperature measurements were conducted using the same thermal conditions in an Al_2O_3-SiO_2 investment casting shell mold system. Furthermore, the results were compared with stray grains in directionally solidified components.

Keywords: Ni-based; superalloys; undercooling; shell mold; temperature measurement; stray grains

---

1. Introduction

Driven by the demand of high-efficiency gas turbines, Ni-based superalloys were developed over the last 40 years for high temperature strength, toughness and oxidation resistance. In total, 5–10 alloying elements of up to 40 wt.% [1] are added to the face-centered cubic nickel to effect the typical y/y' microstructure. The addition of rhenium (Re) to the multi-component Ni-based superalloys

drastically increased these high temperature properties at the expense of density, cost, microstructure stability and castability [2]. Despite all this, the higher creep strength [3] and the reduced y'-coarsening rate [4] makes superalloys containing Re desirable.

The solidification of Ni-based superalloys usually begins with the formation of supersaturated, austenitic y-nickel followed by a solid state phase transformation to the y and intermetallic L_{12} y'-Ni_3Al phase [5]. The micro-segregation of aluminum (Al) and titanium (Ti) leads to a eutectic reaction in the interdendritic regions, resulting in an inhomogeneous, as-cast microstructure of y/y' dendrites and eutectic. Re is an alloying element that has an especially high micro-segregation coefficient, and effects the solidification of Ni-based superalloys.

The well-established directional solidification (DS) and single crystal (SX) technology for aeronautical engines was recently transferred to stationary gas turbines. However, controlling the casting process for the larger blades is challenging and leads to significant numbers of first-stage blade rejects. Due to the use of modern superalloys in power-generation turbines, the castability of large single crystal casting parts gains importance. One of the major casting defects is stray grains featuring high angle gain boundaries (HAGB).

During directional solidification, areas with diameter changes perpendicular to the growth direction can be highly undercooled due to the curvature of the liquidus isotherm [6]. When a critical value of the undercooling is reached, heterogeneous nucleation commences at the inner surface of the ceramic shell mold [7]. As a consequence of this, superalloys with high undercoolability are less prone to stray grains and the reject rate of castings is lower. The undercoolability of a superalloy depends on the following characteristics:

- Chemical composition: Assuming homogeneous nucleation, the undercoolability of nickel alloys depends on the chemical composition of the melt [8–11].
- Process parameters: The supercooling of a melt depends on the process parameters, especially the cooling rate. Usually, higher values of undercooling are obtained with high cooling rates.
- Nucleation mechanism: Melts can be highly undercooled if homogeneous nucleation occurs. This can be achieved using containerless levitation or drop tube experiments [12]. For pure nickel, undercooling values of ΔT = 341–480 K [13,14] were obtained. In the industrial Bridgman process, undercooled zones are usually near the inner shell mold surface, and heterogeneous nucleation lowers the undercooling of the melt. In classical nucleation theory [15], the contact angle Θ correlates with the interface energy between the ceramic substrate and melt. A low contact angle means good wetting and low interface energy. As a consequence, low undercoolabilities for low contact angles are achieved [16].
- Chemical reactions: To produce high-quality large SX gas turbine blades, it is essential to use shell mold systems with sufficiently high temperature properties. Usually, silica-sol-binder and different fractions of ceramic filler are used for the ceramic slurry of the front coating to ensure dimension accuracy, shell mold strength and a stable investment casting process. Contact angle measurements between different ceramics and superalloys show limited chemical reactions between the melt and ceramics containing SiO_2 [17,18].

In this research project, different Ni-based alloys were investigated under industrial process conditions to identify the relationship between melt undercooling and stray grains in three Ni-based alloys.

2. Experimental Section

2.1. Materials

The binary Ni-Re 9 wt.% alloy was manufactured by Sunrelier Metal Co. (Shanghai, China), Limited, and was alloyed with pure 99.9% Ni to produce Ni-Re 4 wt.% and Ni-Re 2 wt.% alloys. CMSX-6 produced by CM-Group and Ni-Re 9 wt.% was combined for Alloy1–Alloy3. The alloys were analyzed using EDX area scans, and the resulting chemical compositions are listed in Table 1.

Table 1. Chemical composition of Ni-based alloys in wt.%.

Name	Ni	Re	Co	Cr	Mo	Al	Ti	Ta	Total
CMSX-6	bal.	-	5.6 ±0.2	10.5 ±0.3	3.5 ±0.2	4.6 ±0.1	4.9 ±0.1	2.2 ±0.3	31.3
Alloy1	bal.	1.2 ±0.2	4.9 ±0.2	9.1 ±0.3	3.1 ±0.2	4.0 ±0.1	4.3 ±0.1	1.9 ±0.3	28.5
Alloy2	bal.	2.3 ±0.2	4.2 ±0.2	7.8 ±0.3	2.6 ±0.2	3.4 ±0.1	3.7 ±0.1	1.6 ±0.3	25.6
Alloy3	bal.	3.5 ±0.2	3.5 ±0.2	6.4 ±0.3	2.2 ±0.2	2.8 ±0.1	3.0 ±0.1	1.4 ±0.3	22.8
Ni2Re	97.7	2.3 ±0.2	-	-	-	-	-	-	-
Ni4Re	95.4	4.6 ±0.2	-	-	-	-	-	-	-
Ni9Re	90.9	9.2 ±0.2	-	-	-	-	-	-	-

2.2. Shell Mold Design and Manufacture

Slurry-coated alumina tubes were inserted into the wax model. The shell molds were manufactured by conventional investment casting using commercial sol-silica-based binder, Al_2O_3 filler and Al_2O_3 stucco material. The shell mold system was composed of two different slurries (front and back-up slurry). The front coating was built up from slurry of 5.3 wt.%. SiO_2 and fine (0.12–0.25 mm diameter) high-purity alumina sand. The intermediate coatings were composed of a slurry of 7.4 wt.%. SiO_2 and fine- and medium-grained (0.25–0.5 mm diameter) alumina. The back-up coatings were built up from a slurry of 7.4 wt.%. SiO_2 and coarse alumina sand (0.5–1.0 mm diameter). The shell molds, having an average shell thickness of 6 mm, were dewaxed in a steam autoclave at 7 bar and then sintered in a firing furnace at 1250 °C.

2.3. Casting Set-Up and Temperature Measurements

The temperature measurements were conducted in a vacuum furnace made by ALD Vacuum Technologies GmbH (Hanau, Germany). Using the shell mold set-up illustrated in Figure 1, three different alloys can be investigated simultaneously. The alloys having a weight of 200 g were placed in the shell mold and melted by heating to 1550 °C. After reaching the target temperature, a dwell time of 10 min was allowed to ensure complete melting. For each alloy, temperature measurements were taken by locating four type B (Pt-6Rh/Pt-30Rh) thermocouples in the center of a sphere with a diameter of 10 mm. In a previous work, Ma *et al.* [19] specified a relationship between the undercoolability and the cooling rates of commercial superalloys. For lower cooling rates, lower undercooling values were obtained. Consequently, in this work, the temperature measurements were conducted using a symmetrical arrangement of thermocouples to obtain similar cooling rates for all specimens. As shown

in Figure 2, the heating program of the resistance heaters consists of four cycles with heating and cooling rates of 20 K/min for temperatures between 1200 ℃ and 1550 ℃.

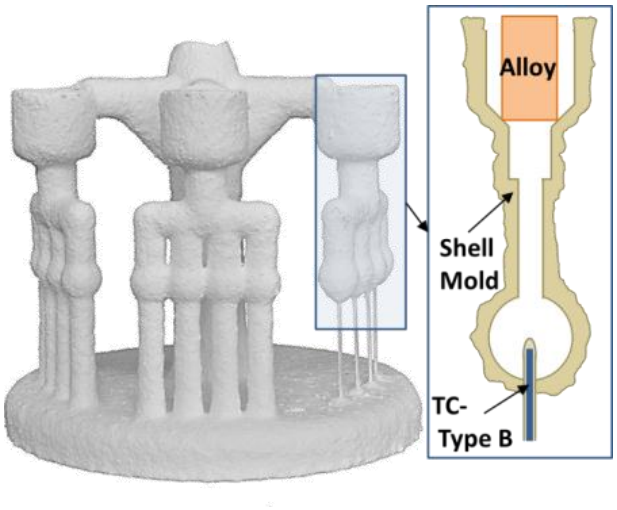

Figure 1. Shell mold for three different alloys furnished with type B thermocouples. The temperature measurement was conducted within a sphere with a diameter of 10 mm.

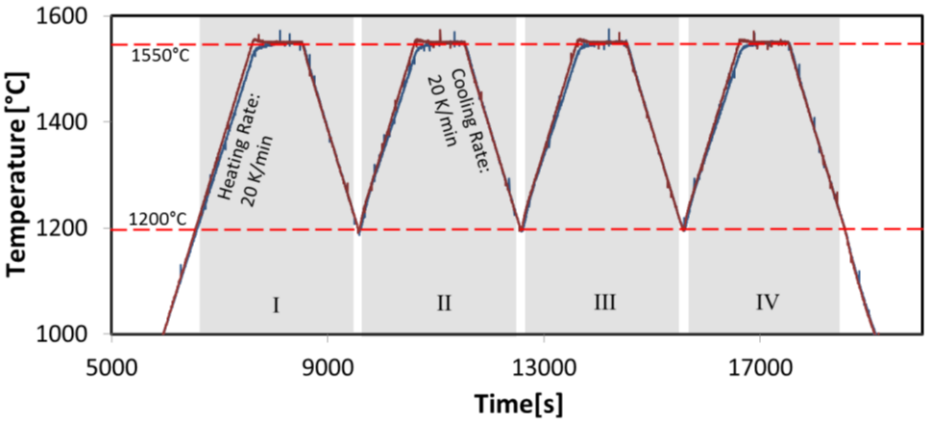

Figure 2. Temperature program for the resistance heater in the vacuum furnace.

2.4. Directional Solidification

Utilizing the Bridgman technology, single crystal (SX) castings were conducted for CMSX-6, Alloy1 and Alloy3 in an industrial-scale Bridgman furnace, consisting of a heating zone, a cooling zone and a vacuum induction unit. A component geometry with abrupt changes of diameter was used to simulate the transition from blade to platform of turbine blades. The dimensions of the platforms, the shell mold design and a schematic illustration of the Bridgman process are shown in Figure 3. Die grain selection was induced with a starter block for columnar solidification and a helix. For the process, the pouring temperature of the melt and the shell mold temperature were adjusted to 100 ℃ superheat for each alloy (Table 2). All castings occurred in a vacuum.

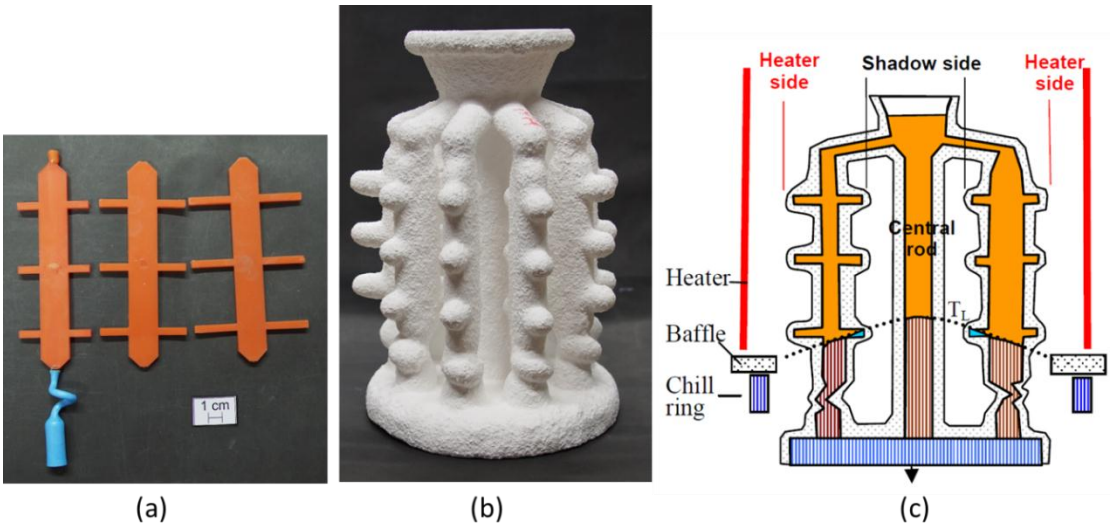

Figure 3. (**a**) Wax model of the components with platform dimensions of 15 mm, 20 mm and 30 mm; (**b**) Shell mold for single crystal solidification; (**c**) Schematic illustration of the curved liquidus isotherm in a Bridgman furnace with the shadow effect to the center column of the shell mold [7].

Table 2. Applied process parameters for the SX castings.

Alloy	Shell Mold Temperature	Pouring Temperature of the Melt	Withdrawal Velocity
CMSX-6	1430 ℃	1430 ℃	v = 3.0 mm/min
Alloy1	1480 ℃	1480 ℃	v = 3.0 mm/min
Alloy3	1500 ℃	1500 ℃	v = 3.0 mm/min

3. Results and Discussion

3.1. Visual Inspection

After removing the shell mold, the samples were visually inspected (Figure 4). While the binary Ni-Re alloys exhibited a glossy surface with easily removable residual ceramic remnants, the surfaces of Alloy1–Alloy3 were dull and the residual ceramic was difficult to remove. These observations indicate a higher reactivity between the alloy elements like Ti and Al of Alloy1–Alloy3 compared to that of binary Ni-Re alloys.

The samples were macroetched with H_2O_2 and HCl to visualize their grain structure. The grain structure for Alloy1 is illustrated in Figure 5 and the grains are denoted with frames. The four big grains points to an initial solidification in each sphere, where the temperature measurement was conducted, and a crystal growth from the bottom to the top of the specimen.

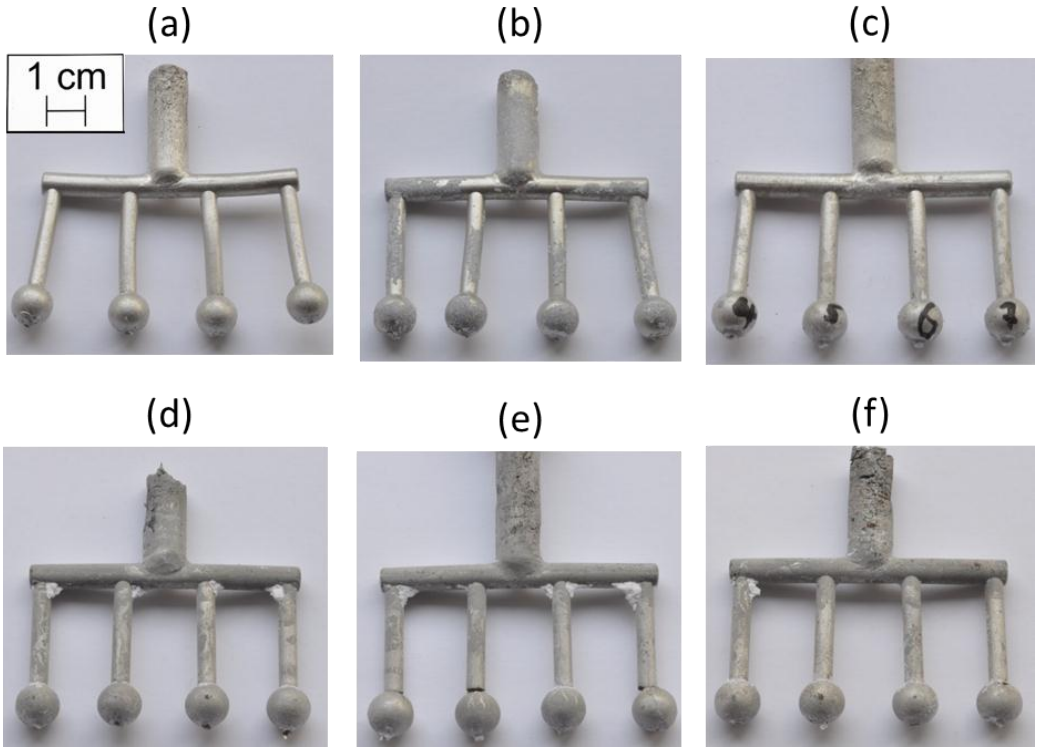

Figure 4. Samples of Ni2Re (**a**), Ni4Re (**b**), Ni9Re (**c**), Alloy1 (**d**), Alloy2 (**e**) and Alloy3 (**f**) after the temperature measurements. The shell mold was removed mechanically.

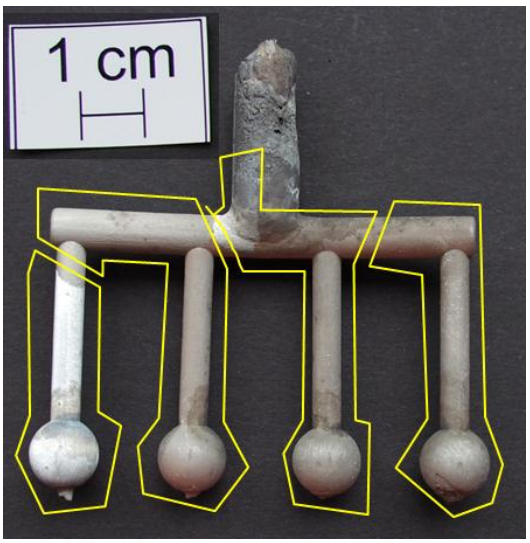

Figure 5. Macroetched sample of Alloy1. The grain structure is denoted by frames.

In Figure 6, the Ni9Re specimen was investigated with computer tomography. While there is a fine dendritic structure with some grains in the sphere, above the sphere coarse dendrites are visible (d). The fineness of the microstructure in the sphere increases from (c) over (b) to (a). Due to the strong micro-segregation of Re to the dendritic area of the microstructure, a density difference between dendrites and interdendritic zones could only be seen for the sample with the highest Re content.

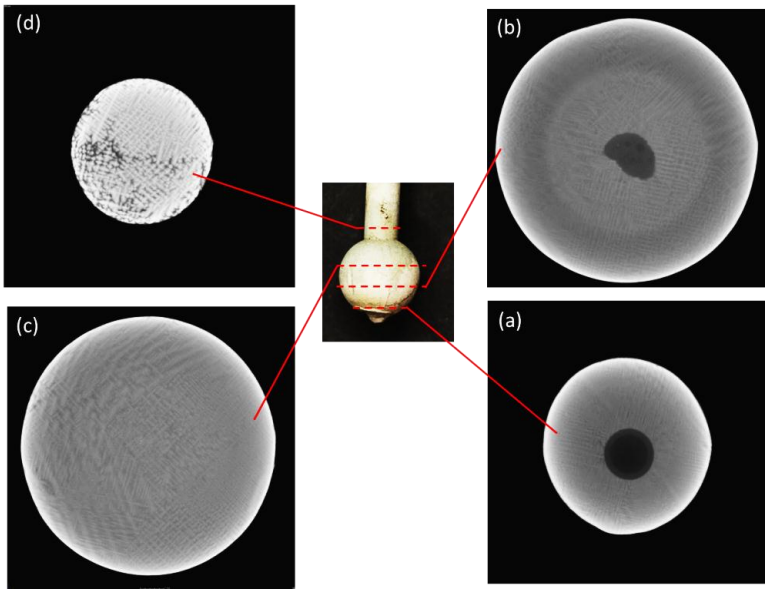

Figure 6. Intersections of the Ni9Re sample recorded with computer tomography. In (**a**), (**b**) and (**c**) a fine dendritic microstructure in the sphere is shown. In (**d**) a coarse microstructure above the sphere is visible.

3.2. Temperature Measurement

In the first heating cycle the alloys have to melt and run in the shell mold, resulting in three measurement cycles. A typical temperature curve for one alloy is shown in Figure 7. If one of the four thermocouples showed unreliable temperature measurements, then these were not considered during the data evaluation.

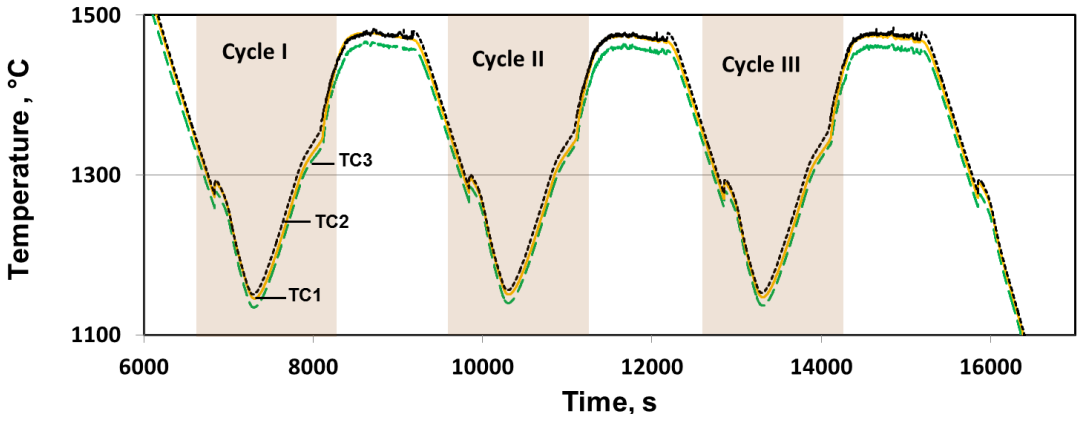

Figure 7. Temperature measurements for one alloy, three different thermocouples and three thermo-cycles.

The liquidus temperature T_L is measured during heating and identified with a maximum in the derivative curve (dT/dt). The critical undercoolability (ΔT_U) of an alloy is the ability to remain liquid below the melting point, and can be specified as the statistical average under certain experimental conditions comparable to those of the shell mold system or thermal conditions. In Figure 8, the undercooling temperatures T_N are measured during cooling and identified with a maximum in the

derivative curve. The cooling rate of all four thermocouples prior to solidification lay between 18.9–19.3 K/min for each alloy.

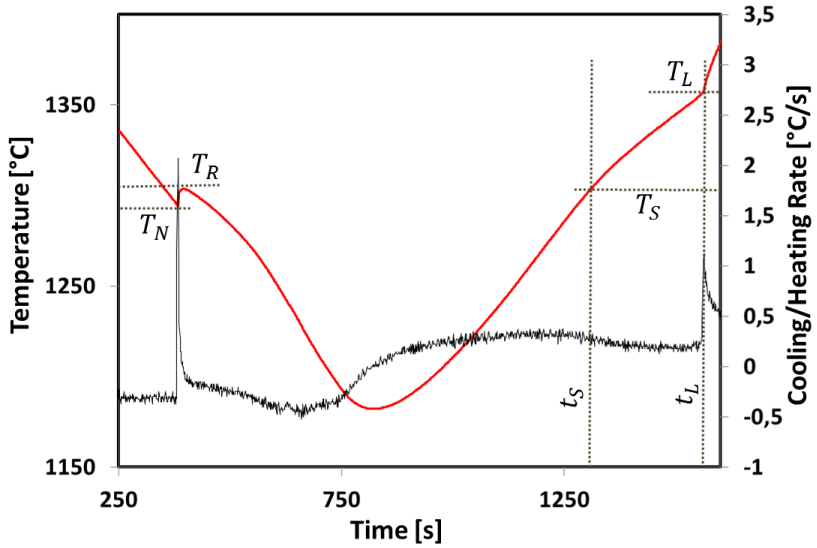

Figure 8. Measurement of the undercooling in one cooling and heating cycle.

The temperature interval (ΔT_{MI}) for melting results from Equation (1).

$$\Delta T_{MI} = T_L - T_S \quad (1)$$

The experimental data and the calculated temperatures for solidus temperature (T_S) and liquidus temperature (T_L) are listed in Table 3. The measured values are consistently lower than the calculated values. The calculated and the experimental values of the solidification interval decrease for Alloy1–Alloy3, while the solidification interval increases for Ni2Re to Ni9Re. The calculated values assume equilibrium states and the experimental values are non-equilibrium states with cooling and heating rates of 20 K/min. For this reason, the experimentally determined solidification intervals are consistently wider.

Table 3. Calculated temperatures using temperature data for the different alloys from the literature, and measured data.

Name	T_S (℃)	T_L (℃)	Solidification Interval (℃)	Experimental T_S (℃)	Experimental T_L (℃)	Melting Interval (℃)
Alloy1	1324.1	1366.4	42.4	1296	1360	64
Alloy2	1353.9	1389.0	35.1	1315	1372	57
Alloy3	1380.0	1412	32	1350	1400	50
Ni2Re[20]	1460	1465	5	1428	1453	25
Ni4Re[20]	1470	1490	20	1435	1469	34
Ni9Re[20]	1490	1530	40	1456	1505	49

The critical undercooling values ΔT_U are calculated using Equation (2). For each thermocouple, three ΔT_U values are recorded.

$$\Delta T_U = T_L - T_N \quad (2)$$

Figure 9 summarizes the measured undercooling data for the binary alloys. Due to the high standard deviation (SD) for all the alloys, no definite relationship can be derived between undercooling and alloy composition. However, one can assume a tendency for lower undercooling with higher Re content. The average undercooling ΔT_U values for Ni2Re, Ni4Re and Ni9Re were 44 K (SD: 7.4 K), 23 K (SD: 4.7 K) and 29 K (SD: 10.6 K), respectively.

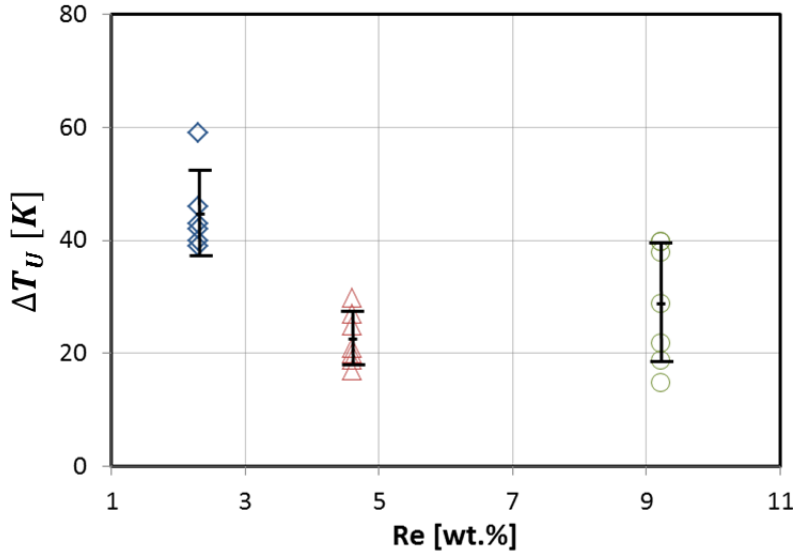

Figure 9. Critical undercooling ΔT_U of the binary Ni-Re alloys.

Figure 10 shows the results for Alloy1–Alloy3. The average undercooling ΔT_U values for CMSX-6, Alloy1, Alloy2 and Alloy3 were 117.9 K (SD: 5.1 K), 56 K (SD: 7.8 K), 82 K (SD: 7.5 K) and 52 K (SD: 4.8 K), respectively. Compared to the binary alloys, CMSX-6 and Alloy1–Alloy3 exhibit higher undercooling abilities. This difference in undercooling can only be attributed to the chemical composition of the alloys since the process conditions and the shell mold properties were identical for each alloy.

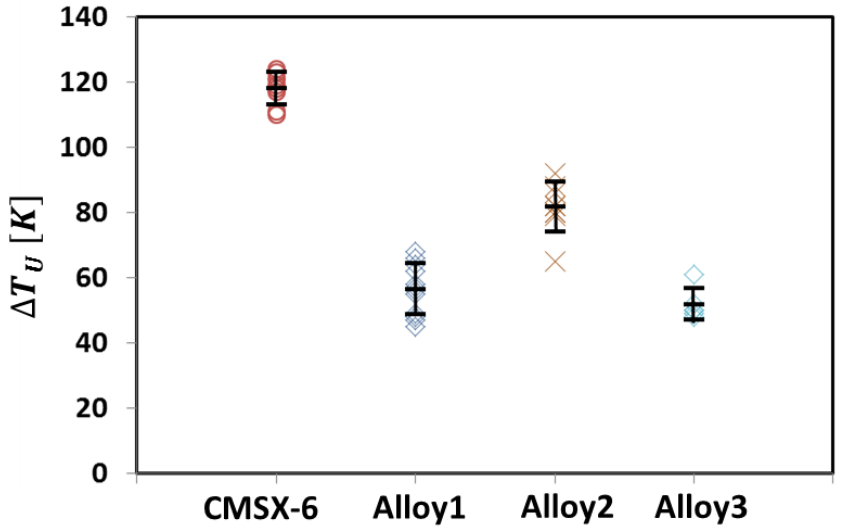

Figure 10. Critical undercooling ΔT_U of Alloy1, Alloy2 and Alloy3.

3.3. Experimental Results of the SX Castings

The undercoolability is particularly important for the single crystal casting of turbine blades. In Figure 11, the single crystal solidification of a dummy blade is schematically illustrated. One side of the turbine blade is oriented towards the heaters (heater side) and the opposite side faces the middle column of the shell mold (shadow side).

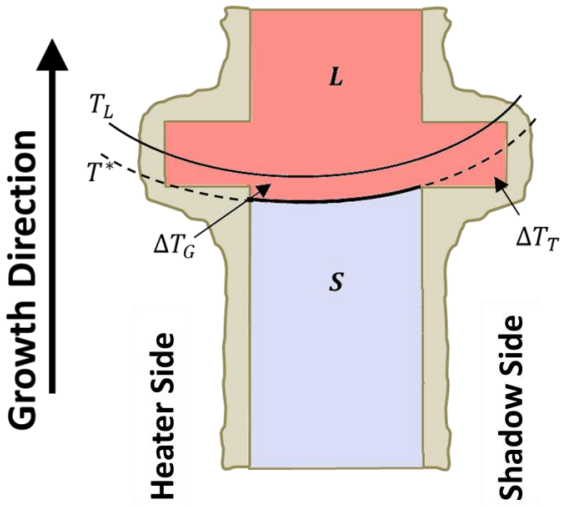

Figure 11. Schematic illustration of the thermal conditions in a dummy turbine blade during transition of the solidification front from blade to platform area. T_L: curved liquidus isotherm; T^*: temperature of the undercooled solidification front; ΔT_G: growth supercooling; ΔT_T: thermal undercooled melt.

In the area of the transition from blade to platform, a zone of thermal undercooled melt ΔT_T appears on the shadow side of the blade due to a curved liquidus isotherm. The curvature of T_L depends on the process parameters (withdrawal velocity, heater temperature and temperature gradient), geometric factors (shell mold thickness and turbine blade geometry) and thermo-physical properties of the superalloy and the shell mold (thermal conductivity). If ΔT_T exceeds ΔT_U, the melt will heterogeneously nucleate on the internal contour of the given shell mold.

Notably, the curvature of the liquidus isotherm depends on the thermal conductivity $\lambda(T)$ of the melt and the solid phases of the alloy. In addition to this, the thermal conductivity is composed of the product of the thermal diffusivity, the heat capacity and the density of the alloy, and is influenced by the chemical composition of the alloy. Therefore, both ΔT_T and ΔT_U are related to the chemical composition and have to be measured to predict the stray grain susceptibility of a SX superalloy.

Figure 12 shows the macroetched grain structure of two blade geometries (30 mm) of CMSX-6 with no stray grains and Alloy3 with stray grains in the platforms. The metallographic examination exhibits significant differences in stray grain number on the heater side and the shadow side of all components.

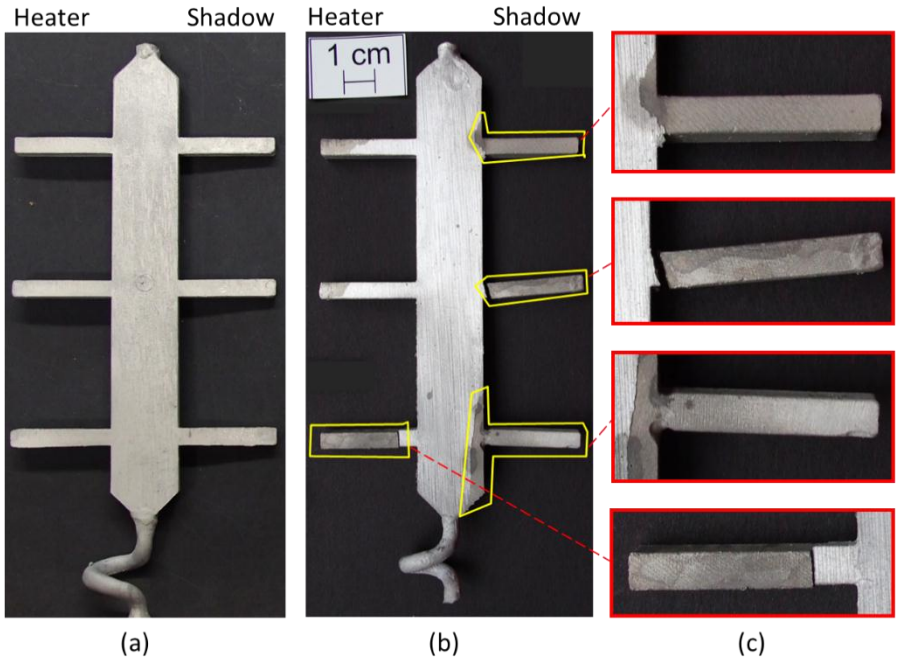

Figure 12. Typical macrostructure of directionally solidified samples: (**a**) CMSX-6; (**b**) Alloy3; (**c**) Magnification of stray grains in the platforms.

In order to evaluate the stray grain formation, the volume ratio of stray grains in the platforms is defined as the stray grain quota (*Q*v). The higher the quota, the more stray grains there are in the platform up to a value of 1, where all extremities are occupied by stray grains. A total of 18 platforms for each alloy and each platform type were examined. In Figure 13, a decrease in *Q*v for lowering the platform dimensions in all investigated alloys arises. Here, the thermal undercooling ΔT_T of the melt is higher in the longer extremities and the critical undercoolability ΔT_U until nucleation can be exceeded.

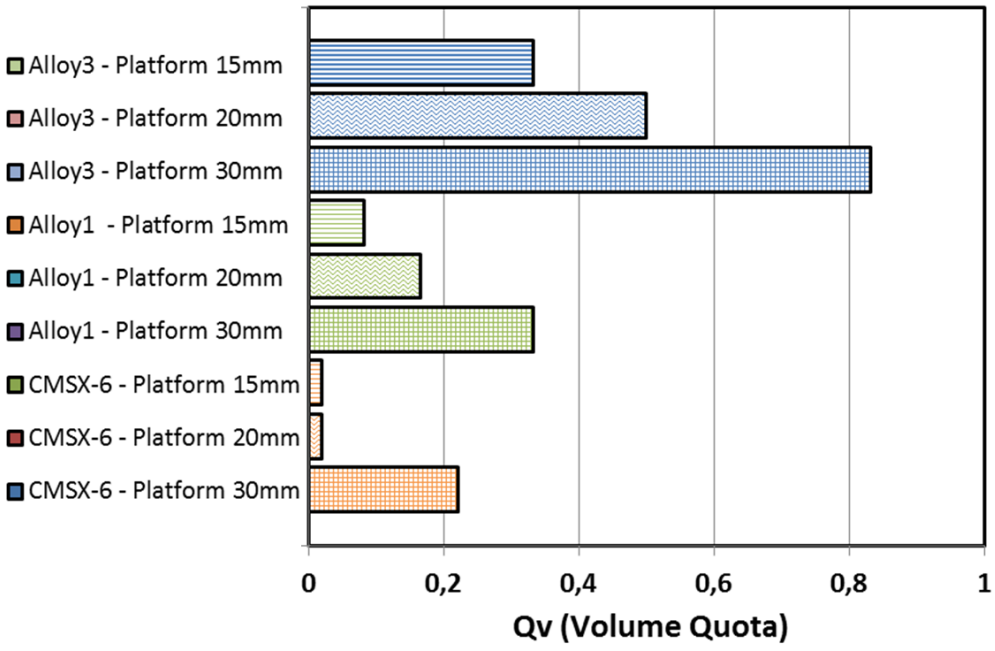

Figure 13. Statistical volume quota *Q*v of stray grains with different platform dimensions of CMSX-6, Alloy1 and Alloy3.

It can be observed, that the tendency of stray grain formation decreases from Alloy3 over Alloy1 to CMSX-6. A comparison between the measured critical undercooling values and the *Q*v values shows high critical ΔT_U and low *Q*v values. Therefore, a direct correlation between critical undercoolability of an alloy and stray grain formation in platforms during SX solidification can be made.

The lower ΔT_U values of the binary Ni-Re alloys compared to the multicomponent alloys have to be critically reviewed und further investigated. There are different explanations from the author's view:

- Alloying elements of the multicomponent alloys limit the atomic movement in the melt which leads to a hindrance in heterogeneous nucleation.
- Superalloys have highly controlled melt treatments which include the removal of oxides, nitides and other impurites. During alloying CMSX-6 with the binary Ni9Re alloy, a chemical componet besides Nickel or Rhenium was inserted and lowered the critical undercoolability ΔT_U considerably.
- Rhenium is an alloy element in Ni-based alloys that decreases the critical undercoolability ΔT_U.

4. Conclusions

The critical undercoolability ΔT_U was measured for seven different alloys in a vacuum furnace using an Al_2O_3-SiO_2 investment casting shell mold system under identical thermal conditions. Furthermore, three alloys were directionally solidified with the same investment casting shell mold system to investigate the stray grain formation in components with platforms. A comparison between ΔT_U and *Q*v showed that alloys with a high critical undercoolability have a low *Q*v value and therefore are unresponsive to stray grains.

Acknowledgments

This work was financially supported by the Deutsche Forschungsgemeinschaft (German Research Foundation) (DFG) through Project No. BU 1072/33-1.

Author Contributions

Samuel Bogner wrote the paper and analyzed the temperature measurements. Marcel Müller was a student who prepared the Ni-based alloys. Elvira Ivanova carried out the experimental set-up. All results were discussed with Fu Wang and A. Bührig-Polaczek. D. Ma supervised and revised the paper.

Conflicts of Interest

The authors declare no conflict of interest.

References

1. Pollock, T.M.; Tin, S. Nickel-based superalloys for advanced turbine engines: Chemistry, microstructure and properties. *J. Propul. Power* **2006**, *22*, 361–374.
2. Caron, P.; Khan, T. Evolution of Ni-based superalloys for single crystal gas turbine blade applications. *Aerosp. Sci. Technol.* **1999**, *3*, 513–523.

3. Blavette, D.; Caron, P.; Khan, T. An atom probe investigation of the role of rhenium additions in improving creep resistance of Ni-base superalloys. *Scr. Metall.* **1986**, *20*, 1395–1400.
4. Giamei, A.; Anton, D. Rhenium additions to a Ni-base superalloy: Effects on microstructure. *Metall. Trans. A* **1985**, *16*, 1997–2005.
5. Hobbs, R.; Tin, S.; Rae, C. A castability model based on elemental solid-liquid partitioning in advanced nickel-base single-crystal superalloys. *Metall. Mater. Trans. A* **2005**, *36*, 2761–2773.
6. Ter Vehn, M.M.; Dedecke, D.; Paul, U.; Sahm, P. Undercooling related casting defects in single crystal turbine blades. *Superalloys* **1996**, doi:10.7449/1996/Superalloys_1996_471_479.
7. Ma, D.; Wu, Q.; Hollad, S.; Bührig-Polaczek, A. Investigation on the asymmetry of thermal condition and grain defect formation in the customary directional solidification process. *IOP Conf. Ser. Mater. Sci. Eng.* **2012**, doi:10.1088/1757-899X/27/1/012037.
8. Eckler, K.; Norman, A.; Gärtner, F.; Greer, A.; Herlach, D. Microstructures of dilute Ni-C alloys obtained from undercooled droplets. *J. Cryst. Growth* **1997**, *173*, 528–540.
9. Li, J.F.; Liu, Y.C.; Lu, Y.L.; Yang, G.C.; Zhou, Y.H. Structural evolution of undercooled Ni-Cu alloys. *J. Cryst. Growth* **1998**, *192*, 462–470.
10. Li, J.F.; Jie, W.Q.; Yang, G.C.; Zhou, Y.H. Solidification structure formation in undercooled Fe-Ni alloy. *Acta Mater.* **2002**, *50*, 1797–1807.
11. Assadi, H.; Barth, M.; Greer, A.L.; Herlach, D.M. Kinetics of solidification of intermetallic compounds in the Ni-Al system. *Acta Mater.* **1998**, *46*, 491–500.
12. Herlach, D.M. Containerless undercooling and solidification of pure metals. *Annu. Rev. Mater. Sci.* **1991**, *21*, 23–44.
13. Willnecker, R.; Herlach, D.; Feuerbacher, B. Containerless undercooling of bulk Fe-Ni melts. *Appl. Phys. Lett.* **1986**, *49*, 1339–1341.
14. Gomersall, D.; Shiraishi, S.; Ward, R. Undercooling phenomena in liquid metal droplets. *J. Aust. Inst. Met.* **1965**, *10*, 220–222.
15. Turnbull, D. Kinetics of solidification of supercooled liquid mercury droplets. *J. Chem. Phys.* **1952**, *20*, 411–424.
16. Liu, F.; Yang, G. Solidification of superalloy in a SiO_2-ZrO_2-B_2O_3 coating mould. *J. Non-Cryst. Solids* **2001**, *290*, 105–114.
17. Virieux, X.; Desmaison, J.; Labbe, J.; Gabriel, A. Interaction between two Ni-base alloys and oxide ceramics: SiO_2, ZrO_2, HfO_2, Al_2O_3. *Mater. Sci. Forum* **1997**, *251–254*, 925–934.
18. Valenza, F.; Muolo, M.; Passerone, A. Wetting and interactions of Ni-and Co-based superalloys with different ceramic materials. *J. Mater. Sci.* **2010**, *45*, 2071–2079.
19. Ma, D.; Wu, Q.; Bührig-Polaczek, A. Undercoolability of superalloys and solidification defects in single crystal components. *Adv. Mater. Res.* **2011**, *278*, 417–422.
20. Okamoto, H. Ni-Re (nickel-rhenium). *J. Ph. Equilib. Diffus.* **2012**, *33*, 346.